RSC Advances

PAPER

View Article Online
View Journal | View Issue

Cite this: *RSC Adv.*, 2024, **14**, 12030

Alkalized MXene/carbon nanotube composite for stable Na metal anodes†

Weisong Meng, Bo Wang, Junkai Zhao, Guilin Jiang, Chenxiao Chu * and Feipeng Cai*

Ti_3C_2 MXenes are emerging 2D materials and have attracted increasing attention in sodium metal anode fabrication because of their high conductivity, multifunctional groups and excellent mechanical performances. However, the severe self-restacking of Ti_3C_2 MXenes is not conducive to dispersing Na^+ and limits the function of regulating sodium deposition. Herein, an alkalized MXene/carbon nanotube (CNT) composite (named A–M–C) is introduced to regulate Na deposition behavior, which consists of $Na_3Ti_5O_{12}$ microspheres, Ti_3C_2 MXene nanosheets and CNTs. Ti_3C_2 MXene nanosheets with large interlayer spaces and "sodiophilic" functional groups can provide abundant active sites for uniform nucleation and deposition of Na. Plenty of nanosheets are grown on the surface of the microsphere, thereby reducing the local current density, which can guide initial Na nucleation and promote Na dendrite-free growth. Furthermore, CNTs increase the electrical conductivity of the composite and achieve fast Na^+ transport, improving the cycling stability of Na metal batteries. As a result, at a capacity of 1 mA h cm^{-2}, the A–M–C electrode achieves a high average coulombic efficiency (CE) of 99.9% after 300 cycles at 2 mA cm^{-2}. The symmetric cells of A–M–C/Na provide a long cycling life of more than 1400 h at 1 mA cm^{-2} with a minimal overpotential of 19 mV at an areal capacity of 1 mA h cm^{-2}. The A–M–C/Na//NVP@C full cell presents a high coulombic efficiency of 98% with 100 mA g^{-1} in the first cycle. The strategy in this work provides new insights into fabricating novel MXene-based anode materials for dendrite-free sodium deposition.

Received 29th February 2024
Accepted 25th March 2024

DOI: 10.1039/d4ra01572j

rsc.li/rsc-advances

1. Introduction

Sodium metal anodes have attracted extensive attention owing to their high theoretical capacity (1165 mA h g^{-1}) and low redox potential (2.71 V *versus* the standard hydrogen electrode) as well as the high natural abundance and low cost of Na resources.[1–3] More attractively, sodium metal anodes have been successfully applied in next-generation high-energy-density battery systems such as Na–S, Na–O_2 and Na–CO_2 batteries; these Na-based batteries possess theoretical specific energies that are about two times higher than that of Li-ion batteries.[4–7] However, the practical adoption of sodium metal anodes is still hindered by Na dendrite formation and the high chemical reactivity between metallic Na and electrolytes, resulting in low coulombic efficiency, poor cycling stability and even severe potential safety hazards.[8–10] Various strategies have been devoted to solving these problems, such as adding additives to the electrolyte,[11–14] constructing artificial SEI films,[15–17] employing an artificial solid electrolyte interphase,[18–21] and designing a deposition framework.[22–26] Notably, stable host construction is a practical, scalable, and effective method to guide the homogeneous nucleation and growth of Na on the surface of Na metal anodes. Among them, MXenes as outstanding Na deposition frameworks have become a research hotpot.

MXenes, two-dimensional (2D) transition metal carbides, have recently been regarded as promising host materials owing to their unique physicochemical properties.[27,28] The synthesis of MXenes is generally achieved by etching "A" element layers (mostly Al) from a layered MAX precursor using hydrofluoric acid (HF) or combinations of fluoride salts and acids (HCl + LiF).[29,30] MXenes share a general chemical of $M_{n+1}X_nT_x$, where M is an early transition metal such as Ti, V, and Cr; X is C or N; n = 1, 2 or 3; and T_x denotes different surface terminations such as O, F and OH functional groups.[31–33] O, F and OH functional groups can induce uniform ion flux and achieve dendrite-free metal deposition. Moreover, MXene shows other exceptional properties in terms of high surface area, and good mechanical structure.[34–36] Usually, $Ti_3C_2T_x$ is by far the most studied and well-understood and has been used in the fields of sodium metal anodes. For instance, Luo *et al.* designed Ti_3C_2 MXene with Sn^{2+} pillared acting as a stable substrate for high-performance dendrite-free Na metal anode,[37] in which the Sn^{2+} intercalation between Ti_3C_2 layers takes advantage of the

Energy Institute, Qilu University of Technology (Shandong Academy of Sciences), Jinan, 250014, China. E-mail: chucx@sderi.cn; caifp@sderi.cn

† Electronic supplementary information (ESI) available. See DOI: https://doi.org/10.1039/d4ra01572j

"pillar effect" to endow the Ti_3C_2 with larger interlayer space to accommodate the deposited Na, contributing to uniform Na deposition. The authors further reported 1D/2D $Na_3Ti_5O_{12}$-MXene nanostructures consisting of $Na_3Ti_5O_{12}$ nanowires grown between the MXene nanosheets.[38] The unique nanostructures not only provide abundant Na nucleation sites but also effectively confine Na nucleation in the interconnected nanochannels, delivering outstanding cycling performance at high current densities and high capacities.

Inspired by these studies, herein, we introduced 1D/2D/3D hybrid nanostructures consisting of $Na_3Ti_5O_{12}$ microspheres, Ti_3C_2 MXene nanosheets and CNTs to regulate Na deposition. Larger interlayer gaps and "sodiophilic" functional groups in Ti_3C_2 MXene nanosheets offer a wealth of active sites for the consistent nucleation and deposition of Na. Plenty of nanosheets are grown on the surface of microspheres to reduce the local current density, which can guide the initial Na nucleation and promote Na dendrite-free growth. The presence of CNTs further enhances the electrical conductivity of the composites, improving the cycling stability of the battery. The results indicate that the A–M–C electrode acquires a high average coulombic efficiency (CE) of 99% after 300 cycles at 2 mA cm^{-2} with a capacity of 1 mA h cm^{-2}. At an areal capacity of 1 mA h cm^{-2}, the symmetric cells of A–M–C deliver a long-term cycling life (300 cycles) at 1 mA cm^{-2} with a small hysteresis of 20 mV. The A–M–C/Na//NVP@C full cell presents a stable cycling performance and good capacity retention.

2. Results and discussion

A schematic of the fabricated strategy for 1D/2D/3D hybrid nanostructures is exhibited in Fig. 1a. First, the precursor Ti_3AlC_2 was etched by HCl and LiF to obtain Ti_3C_2 MXene. *In situ* generation of sodium titanate microspheres on the surface of Ti_3C_2 MXene under high temperature, high pressure, and low alkalinity conditions. Finally, CNT was added to increase the conductivity of the material. Scanning electron microscopy (SEM) of A–M shows that the microspheres with a diameter of about 1 μm are grown among numerous monolayer MXene clusters (Fig. 1b). It can be clearly seen that the microspheres are formed by stacking a large number of nanosheets (Fig. 1c). When MXene is fully alkaline, the structure of the microspheres can be seen more clearly (Fig. S1a†). The Ti_3C_2 MXene after alkalization treatment has better independence without severe aggregation such as in pristine MXene nanosheets (Fig. S1b†). CNTs are homogeneously distributed in the A–M, forming the 1D/2D/3D/hybrid structures (Fig. 1d). Elemental mapping results verified the homogeneous element distribution of Na, Ti, C, O and F in A–M (Fig. 1e–i).

The elements content and condition of A–M–C were investigated by X-ray diffraction (XRD) and Raman spectra. As shown in Fig. 2a, a strong peak at 9.0° is assigned to the in-plane diffraction (002) of Ti_3C_2 with a *d*-spacing of ~0.98 nm, well consistent with that from the reported literature.[38] In addition, the (002) diffraction peak shifts towards to lower angle compared to that in the untreated Ti_3C_2 MXene,[39,40] which illustrates a larger interlayer spacing. As shown in Fig. 2b, the Raman spectrum of A–M–C displays two characteristic peaks of D bands (1327 cm^{-1}) and G bands (1576 cm^{-1}), I_D/I_G values are determined according to the area ratio of D band to G band is 1.67, which indicates a high defect in A–M–C. Further, the surface chemistry information of the A–M–C was detected by X-ray photoelectron spectroscopy (XPS), and the survey spectrum displayed the presence of C, Ti, O and F elements. High-resolution XPS spectra in the C1s region (Fig. 2c) revealed three main peaks occurring at 281.4, 284.6 and 287.8 eV, which may originate from Ti–C, C–C and C–O, respectively.[41]

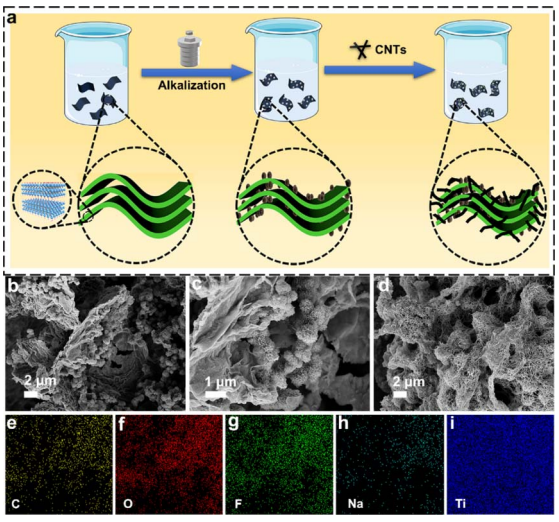

Fig. 1 (a) Schematic illustration of the fabrication steps for the A–M–C. (b and c) SEM images of A–M. (d) SEM images of A–M–C and (d–i) corresponding elemental mappings of C, O, F, Na and Ti elements.

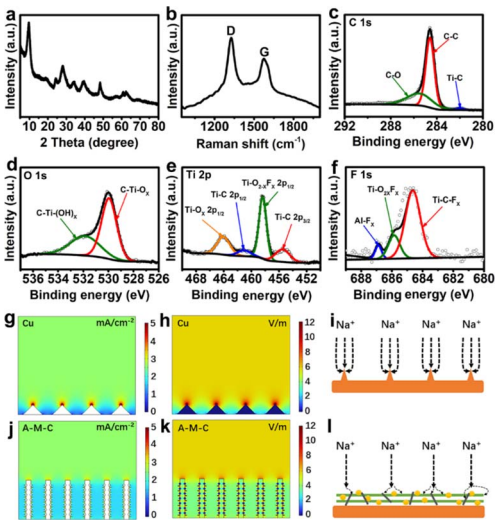

Fig. 2 (a) XRD pattern of A–M–C. (b) Raman spectra of A–M–C. XPS spectra of (c) C 1s, (d) O 1s, (e) Ti 2p and (f) F 1s. COMSOL Multiphysics simulation results of (g and h) the current density distribution and (j and k) the electric field distribution near the surface of the Cu and A–M–C electrodes. (i and l) Schematic of the growth modes for Na plating in bare Cu and A–M–C.

Moreover, as shown in Fig. 2d, the O 1s spectrum shows C–C and C–O peaks at 531.7 and 532.5 eV, respectively. Fig. 2e exhibits Ti 2p peaks at 455.1, 458.7, 461.2 and 464.9 eV that can be assigned to Ti–C $2p_{3/2}$, Ti–O $2p_{3/2}$, Ti–C $2p_{1/2}$ and Ti–O $2p_{1/2}$ peaks, respectively.[42,43] The stronger Ti–O peaks and the weaker Ti–C peaks indicate that the MXene is partly oxidized.[44] Fig. 2f shows the F 1s peaks, indicating the presence of the F element.[45] These abundant functional groups ensure dendrite-free deposition of sodium. In order to demonstrate that more stable sodium metal deposition can be achieved on the A–M–C surface, COMSOL Multiphysics finite element simulation was applied to simulate two electrode surfaces. As shown in Fig. 2g–h and j–k, compared with bare Cu copper, the current density distribution and electric field distribution on the A–M–C surface are more uniform, because of which, A–M–C has a larger specific surface area and abundant functional groups on the surface; these advantages of A–M–C effectively avoid "tip effect", Na^+ is not accumulated on the tip and grown larger, which is an important reason for the realization of sodium dendrite-free deposition. Fig. 2i and l show a schematic of the growth modes for Na plating in the bare Cu and A–M–C.

The Na plating behaviors onto the A–M–C matrix and Cu foil were systematically investigated using a two-electrode cell configuration (CR2032) with 1 M sodium hexafluorophosphate ($NaPF_6$) as the electrolyte. Voltage overshooting was observed at the two working electrodes when sodium plating occurred in both electrode systems, this could be the result of sodium atoms overcoming the nucleation barrier, which is referred to as nucleation overpotential. The Na nucleation overpotential is characterized by the difference between the flat voltage plateau and the lowest point of the voltage dip. At a current density of 0.5 mA cm^{-2} and an areal capacity of 1 mA h cm^{-2}, the initial sodium nucleation overpotential is 25 mV on Cu, compared to 13.5 mV on A–M–C (Fig. 3a), which is mainly due to the significant thermodynamic mismatch between Cu foil and Na and there are strong nucleation overpotentials. The MXene material in A–M–C with functional groups on its surface acts as nucleation sites for Na deposition, lowering the resistance to Na nucleation. To gain a deeper understanding of this phenomenon, electrochemical impedance spectroscopy (EIS) spectra were gathered. As depicted in Fig. S2,† after 10 cycles at a current density of 1 mA cm^{-2} with a deposition capacity of 1 mA h cm^{-2}, the overall impedance of A–M–C anode at ~36 Ω is much lower than that of Cu anode (117 Ω). These results provide a strong rationale for the large overpotential of Cu anode, which can be attributed to the accumulation of a SEI film, as well as its loose and moss-like structure. CNT increases the electrical conductivity of the material, realizing the rapid electron transport, and promoting the dendrite-free growth of sodium. Coulombic efficiency (CE) is a key indicator to assess the sustainability of Na metal batteries, which is defined as the ratio of the amount of the stripped Na to that of plated Na in each cycle. The CE measurement was performed in a half-cell configuration consisting of bare Na paired with different working electrodes (Cu foil and A–M–C). With a current density of 0.5 mA cm^{-2} and an areal capacity of 1 mA h cm^{-2}, A–M–C displays a higher CE and low voltage retardation, obviously

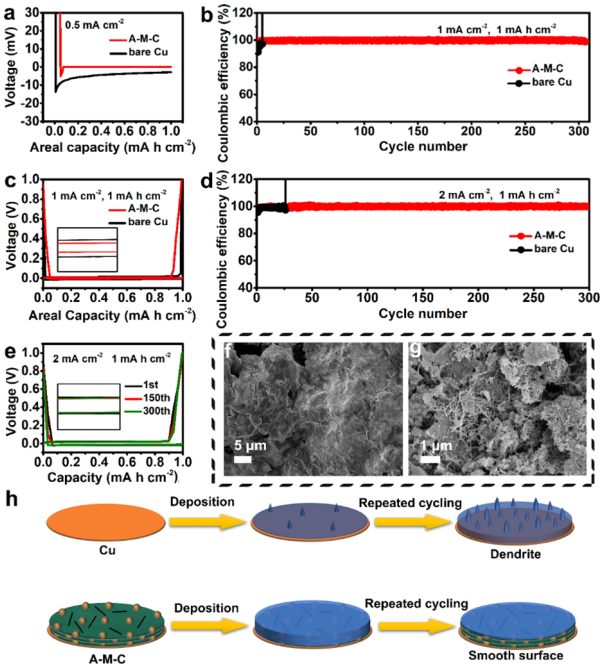

Fig. 3 (a) Initial Na nucleation overpotentials of A–M–C and bare Cu foil at a current density of 0.5 mA cm^{-2}. (b) Comparison of the coulombic efficiency of A–M–C and bare Cu at a current density of 1 mA cm^{-2} for the capacity of 1 mA h cm^{-2}. (c) The corresponding voltage profiles of Na plating/stripping on A–M–C and bare Cu in the first cycle. (d) Comparison of the coulombic efficiency of A–M–C and bare Cu at a current density of 2 mA cm^{-2} for the capacity of 1 mA h cm^{-2}. (e) Typical galvanostatic discharge–charge profiles of the A–M–C electrode at 2 mA cm^{-2} with capacity fixed at 1 mA h cm^{-2}. (f) SEM image of A–M–C after plating Na of 1 mA h cm^{-2}. (g) SEM image of A–M–C after 10 cycles at 1 mA cm^{-2} for a capacity of 1 mA h cm^{-2} Na. (h) Schematic diagrams of Na deposition and repeated cycling in bare Cu and A–M–C.

superior to Cu (Fig. S3 and S4†). In addition, it can be observed that the CE of A–M–C is stable at 99.1% over 300 cycles at a current density of 1 mA cm^{-2} with a deposition capacity of 1 mA h cm^{-2}, and overpotential was only 5 mV (Fig. 3b). From Fig. 3c, it is obvious that bare Cu electrode has a higher overpotential than the A–M–C electrode. In comparison, Cu foil exhibits lower CE with high fluctuation, the average corresponding CE values are 83.7% before 7 cycles at the same condition and get short-circuited. The low CE values of Cu reflect the unstable SEI formed on the electrode interfaces, while the large fluctuation may be ascribed to the "dead Na" formed during the stripping process resulting from the Na dendrites and thus the reconnection of these fractured pieces from previous cycles. As the current density increases to 1 mA h cm^{-2}, the CE of A–M–C is maintained at 99.9% over 300 cycles with the smallest overpotential of 30 mV at a current density of 2 mA cm^{-2} (Fig. 3d) and the plating/stripping curves of A–M–C are still highly coincident (Fig. 3e). The above-mentioned CE test results show that the A–M–C material has structural advantages, which allow the battery to maintain good performance during the cycle. Electrochemical impedance

spectroscopy revealed the interfacial resistance of A–M–C and bare Cu half cell.

To further understand the effects of Na plating, the morphology of A–M–C and Cu foil was imaged following the plating of Na after the first cycle. As shown in Fig. 3f A–M–C displays uniform and planar morphology after Na deposition at 1 mA cm^{-2} with different areal capacities. This can be ascribed to the unique structure and abundant functional groups of A–M–C, which guide the uniform Na nucleation and inhibit dendrite formation. In contrast, a mossy shape is observed for bare Cu after plating 1 mA h cm^{-2} Na, which intends to form fresh SEI and dead Na metal leading to unstable efficiency during the plating process (Fig. S5†). Interestingly, further increasing the plating capacity to 3 mA h cm^{-2}, there is still no dendrite formed on the surface of A–M–C, proving the advantage of its unique structure (Fig. S6†). In addition, morphology characteristics of A–M–C and Cu foil are also explored after several cycles. As expected, mossy dendrites appeared on the Cu foil surface after only 10 cycles, while the A–M–C electrode maintained smooth morphology without dendrite formation after 10 or even 50 cycles (Fig. 3g and S7†). Fig. 3h simulates the deposition and cycle processes of sodium metal in different substrates. The "sodiophilic" properties of the O and F-containing functional groups may benefit from the increased number of active sites on A–M–C for Na deposition, which has a positive effect on lowering the nucleation overpotential. Additionally, as a result of the high specific surface area of the A–M–C skeleton, the local current density during Na deposition can be greatly lowered, minimizing the nucleation overpotential. Since the nucleation size and overpotential are inversely related, homogeneous Na deposition rather than Na dendrites can be produced more easily.

To probe the cycling stability of the A–M–C/Na symmetric cells, two identical A–M–C electrodes were assembled, and bare Na foil symmetric cells served as the control group. Fig. 4a displays the extended voltage profiles of the symmetric cells at 0.5 mA cm^{-2} with 1 mA h cm^{-2} capacity loading. The Na//Na symmetric cell showed low voltage polarization in the first several cycles, however, the cell died due to the suddenly increased voltage polarization and only cycled for 100 hours. This could be due to the dynamic evolution of dendrites that causes the spatial variation of the local reaction kinetics on the electrode surface. In contrast, the A–M–C electrode showed cyclic stability without obvious fluctuations, and the overpotential changed very little as the cycle progressed, indicating the stability of the internal resistance. At the beginning, the A–M–C electrode overpotential was about 12 mV (Fig. 4b), and the overpotential was still only 17 mV after maintaining an ultra-stable cycle of 1700 h, affirming its high stability during prolonged cycling, which can be ascribed to effective suppression of Na dendrites benefiting from the presence of the active sites to control Na nucleation. When the current density was increased to 1 mA cm^{-2} and 2 mA cm^{-2}, stable polarization in the A–M–C electrodes with low average overpotentials of 20 mV and 34 mV can still be achieved at long-term cycles of over 1400 h and over 1200 h, respectively (Fig. 4c, S8 and S9†). Similarly, the bare Na symmetric cell suffered obvious voltage

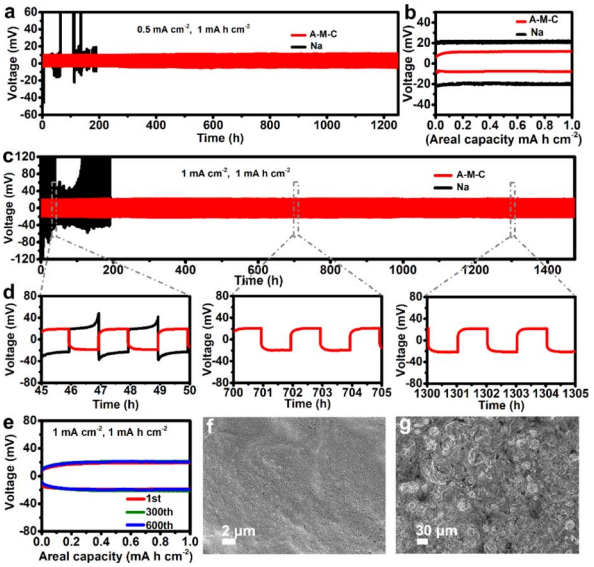

Fig. 4 Voltage profiles of Na metal plating/stripping in A–M–C/Na and Na symmetric cells at (a) 0.5 mA cm^{-2} and (c) 1 mA cm^{-2} with capacity fixed at 1 mA h cm^{-2}. (b) Voltage profiles of A–M–C/Na and Na in the 1st cycle with a capacity of 1 mA h cm^{-2} at 0.5 mA cm^{-2}. (d) Detailed voltage profile of A–M–C/Na. (e) Voltage profiles of A–M–C/Na in different cycles with a capacity of 1 mA h cm^{-2} at 1 mA cm^{-2}. SEM images of (f) A–M–C and (g) Cu planting and stripping after 10 cycles at 1 mA cm^{-2} with a capacity of 1 mA h cm^{-2}.

oscillations shortly afterward, followed by a sudden short circuit. As can be seen in Fig. 4d, in the early cycles, the A–M–C symmetric cell has a lower overpotential than Cu symmetric cell. In the next cycles, the Cu symmetric cell shorted, and the A–M–C symmetrical cell still maintained a stable cycle, indicating that the A–M–C skeleton can significantly improve the stability of the sodium metal anode. Furthermore, SEM was utilized to probe the morphologies of different substrates (A–M–C and bare Na) planting and stripping after 10 cycles at 1 mA cm^{-2} with a capacity of 1 mA h cm^{-2}. Fig. 4f shows that the A–M–C maintains the original structure with little dendrite or "dead Na" on the surface. Similarly, the cycled Na electrode (Fig. 4g) exhibits numerous moss-liked dendrites and fluffy porous "dead Na" which accounts for the increasing polarization observed in Fig. 4c. Overall, according to the above results, it is concluded that the A–M–C substrate can accommodate Na effectively with symmetrical deposition/dissolution and small polarizations, finally improved electrochemical performances.

To explore the possible usefulness of the A–M–C electrode in SMBs, full cells are built and tested (Fig. 5a) with A–M–C@Na serving as the anode and $Na_3V_2(PO_4)_3$@C as the cathode. Fig. 5b shows the voltage profiles of the A–M–C/Na//NVP@C and Na//NVP@C full cell at 100 mA g^{-1} in the first cycle, and Fig. 5c demonstrates the voltage profiles of A–M–C/Na//NVP@C at 100 mA g^{-1} in different cycles. After 660 cycles at 100 mA g^{-1}, the A–M–C/Na//NVP@C complete cell shows a respectable capacity retention of 95.3% and a discharge-specific capacity of 97.32 mA h g^{-1}. On the other hand, the Na//NVP@C complete cell's discharge-specific capacity rapidly decreases to 83 mA h g^{-1}, and after 660 cycles, the capacity retention drops

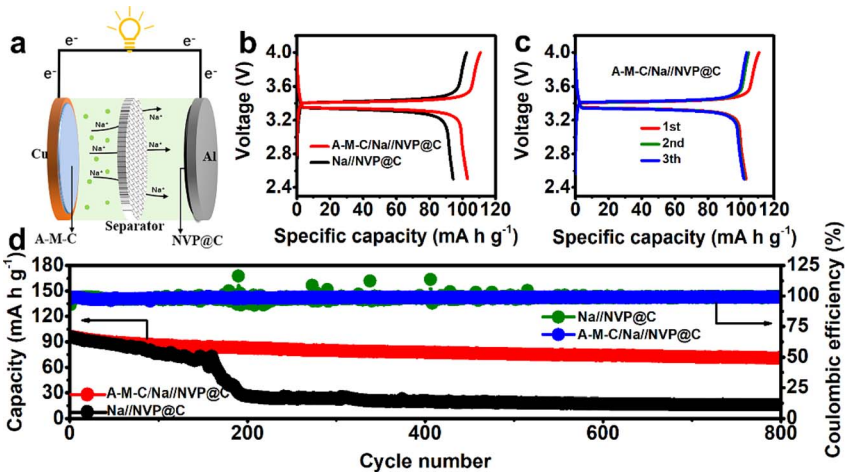

Fig. 5 (a) The schematic illustration of full cells. (b) Voltage profiles of A–M–C/Na//NVP@C and Na//NVP@C cells at 100 mA g^{-1} in the 1st cycle. (c) Voltage profiles of the A–M–C/Na//NVP@C cell at 100 mA g^{-1} in different cycles. (d) Cycling performance and coulombic efficiency of full cells at 100 mA g^{-1}.

to 85% (Fig. 5d). It can also be seen in Fig. 5d that the A–M–C/Na//NVP@C full cell has a high and stable coulombic efficiency (98.7%), while the coulombic efficiency of Na//NVP@C full cell fluctuates, indicating that its poor electrochemical stability. As shown in Fig. S10,† the rate performance of full cells was tested. At the rate of 50 mA g^{-1}, the A–M–C/Na//NVP@C full cell's capacity was 105 mA h g^{-1}, and the capacity of the Na/NVP@C full battery was only 96 mA h g^{-1}; the capacity gap becomes even more apparent as the rate increases, and the difference was the greatest at 500 mA g^{-1} (70 mA h g^{-1} and 50 mA h g^{-1}, respectively). The better electrochemical performance of the A–M–C/Na//NVP@C full cell can be attributed to the structural advantages of the A–M–C skeleton.

3. Conclusions

In summary, we synthesized an A–M–C skeleton with 1D/2D/3D hybrid nanostructures that served as a Na deposition matrix to regulate Na plating behavior. Specifically, the unique structures consisting of $Na_3Ti_5O_{12}$ microspheres, MXene nanosheets and CNTs, the structures of which greatly increased the specific surface area of the material and played an important role in reducing the local current density. The Ti_3C_2 MXene nanosheets with larger interlayer spaces and "sodiophilic" functional groups could provide abundant active sites for uniform nucleation and deposition of Na. Plenty of nanosheets are grown on the surface of the nanosphere to reduce the local current density, which can guide the initial Na nucleation and promote Na dendrite-free growth. Furthermore, CNTs increased the composites' electrical conductivity and achieved fast Na^+ transport, improving the cyclic stability of anodes. Specifically, the half-cells using A–M–C electrodes achieved a high average coulombic efficiency (CE) of 99% after 300 cycles at 2 mA cm^{-2} with a capacity of 1 mA h cm^{-2}. The symmetric cells of A–M–C provide a long cycling life (300 cycles) at 1 mA cm^{-2} with a minimal hysteresis of 20 mV at an areal capacity of 1 mA h cm^{-2}.

4. Experimental section

4.1 Synthesis of few-layered $Ti_3C_2T_x$ suspension

$Ti_3C_2T_x$ was obtained from Ti_3AlC_2 by *in situ* etching method according to the previously reported method. Typically, 1.6 of lithium fluoride (LiF) was added to 20 mL of 9 M HCl solution under stirring. 1.0 g of Ti_3AlC_2 powder was then slowly added to the mixture after the LiF was absolutely dissolved in the solution. The reaction mixture was stirred at 40 °C for 24 h, then centrifuged and washed with distilled water several times until the pH of the supernatant was 6 and further diluted with 200 mL of distilled water. Finally, the diluent was ultrasonically treated under bubbling Ar for 1 h and centrifuged at 3500 rpm for 1 h to obtain the dark green supernatant of a few-layer Ti_3C_2 (20 mg mL^{-1}).

4.2 Synthesis of A–M–C

5 mL Ti_3C_2 suspension mixed with 30 mL DI water and 0.1 g NaOH was dissolved to form a solution and it was followed by the addition of 0.06 mL hydrogen peroxide. After that, the reaction solution was kept at room temperature under continuous stirring for 20 min, then transferred into a 50 mL Teflon-lined stainless-steel autoclave. The autoclave was kept at 140 °C for 8 h. The obtained products were washed with DI water several times and the Ti_3C_2 powder was obtained by freeze-drying technology. Subsequently, CNTs and MXene powder were dissolved in 30 mL DI water and ultrasonically treated for 30 minutes to obtain a homogeneous solution. The A–M–C powder was obtained by freeze-drying technology.

4.3 Material characterization

SEM images and element maps were recorded using a field emission scanning electron microscope (Zeiss Gemini 300, Germany). TEM images were acquired on a transmission electron microscope (JEOL JEM-2100, Japan). X-ray diffraction (XRD) patterns were collected with a graphite monochromator

and Cu Kα X-ray source ($\lambda = 1.5418$ Å) on the Rigaku D/MAX 2500/PC diffractometer. X-ray photoelectron spectroscopy (XPS) was performed using monochromatic Al Kα radiation with an Escalab 250Xi spectrometer (Thermo Scientific, USA). Raman spectra were recorded at room temperature using a Raman spectrometer (Nicolet NEXUS 670, USA). Specific surface area measurements were conducted using a gas adsorption instrument (Micromeritics, ASAP-2460 USA).

4.4 COMSOL simulations

The simulation used the physical field interface of the secondary current distribution in the electrochemistry module of COMSOL Multiphysics software to simulate two electrode surfaces. In terms of material setting, the electrolyte conductivity was set to 0.45 S m^{-1} and the fiber conductivity to 2×10^4 S m^{-1}. The conductivity of the Cu electrode material was 1×10^7 S m^{-1}; in terms of the boundary setting, the ref. 0 V potential was set at the bottom.

4.5 Electrochemical measurements

A–M–C electrodes were typically made by combining A–M–C power and polyvinylidene difluoride (PVDF) at a weight ratio of 8 : 1, *N*-methyl-2-pyrrolidone was then added to create a homogenous slurry, which was then coated onto Cu foil and dried for eight hours at 60 °C in a vacuum environment before being punched into a disc measuring 12 mm in diameter. The electrochemical performances were characterized by assembling A–M–C electrodes in CR2032-type coin cells and using the Neware battery testing system. 1 M sodium hexafluorophosphate (NaPF6) dissolved in diglyme (DEGDME) was employed as an electrolyte. A glass microfiber membrane (Whatman GF-F) was used as a separator.

Conflicts of interest

There are no conflicts to declare.

Acknowledgements

This work was supported by the Natural Science Foundation of Shandong Province (No. ZR2021QB138); The Foundation (No. BG-KFX-01) of Shandong Provincial Key Laboratory of Biomass Gasification Technology, Qilu University of Technology (Shandong Academy of Sciences); The Science, Education and Industry Integration of Basic Research Projects of Qilu University of Technology (Shandong Academy of Sciences) (2023PX007); Talent research project of Qilu University of Technology (Shandong Academy of Sciences) (2023RCKY161); Science and Technology Project of Shandong Province (WST2020010); Talent Project of University and Research Institute of Jinan (2020GXRC044).

References

1 H. Kamath, B. Dunn and J. M. Tarascon, Electrical Energy Storage for the Grid: A Battery of Choices, *Science*, 2011, **334**, 928–935.
2 C. Chu, R. Li, F. Cai, Z. Bai, Y. Wang, X. Xu, N. Wang, J. Yang and S. Dou, Recent advanced skeletons in sodium metal anodes, *Energy Environ. Sci.*, 2021, **14**, 4318–4340.
3 Y. Zhao, K. R. Adair and X. Sun, Recent developments and insights into the understanding of Na metal anodes for Na-metal batteries, *Energy Environ. Sci.*, 2018, **11**, 2673–2695.
4 Y. Wu, Q. Xu, L. Huang, B. Huang, P. Hu, F. Xiao and N. Li, Encapsulation of sulfur in MoS_2-modified metal-organic framework-derived N, O-codoped carbon host for sodium–sulfur batteries, *J. Colloid Interface Sci.*, 2024, **654**, 649–659.
5 Sungjemmenla, C. Soni, S. K. Vineeth and V. Kumar, Chemically tuned nitrogen-doped sulfur host for a reversible and stable room-temperature sodium-sulfur batteries, *J. Energy Storage*, 2024, **75**, 109708.
6 S. M. B. Khajehbashi, L. Xu, G. Zhang, S. Tan, Y. Zhao, L. Wang, J. Li, W. Luo, D. Peng and L. Mai, High-Performance Na-O_2 Batteries Enabled by Oriented NaO_2 Nanowires as Discharge Products, *Nano Lett.*, 2018, **18**, 3934–3942.
7 Z. Tong, S. Wang, M. Fang, Y. Lin, K. T. Tsai, S. Y. Tsai, L. Yin, S. Hu and R. Liu, Na–CO_2 battery with NASICON-structured solid-state electrolyte, *Nano Energy*, 2021, **85**, 105972.
8 H. Wang, E. Matios, J. Luo and W. Li, Combining theories and experiments to understand the sodium nucleation behavior towards safe sodium metal batteries, *Chem. Soc. Rev.*, 2020, **49**, 3783–3805.
9 B. Sun, P. Xiong, U. Maitra, D. Langsdorf, K. Yan, C. Wang, J. Janek, D. Schroder and G. Wang, Design Strategies to Enable the Efficient Use of Sodium Metal Anodes in High-Energy Batteries, *Adv. Mater.*, 2020, **32**, 1903891.
10 C. Ma, T. Xu and Y. Wang, Advanced carbon nanostructures for future high performance sodium metal anodes, *Energy Storage Mater.*, 2020, **25**, 811–826.
11 X. Chen, X. Shen, T. Hou, R. Zhang, H. Peng and Q. Zhang, Ion-Solvent Chemistry-Inspired Cation-Additive Strategy to Stabilize Electrolytes for Sodium-Metal Batteries, *Chem*, 2020, **6**, 2242–2256.
12 X. Xiong, Q. Zhou, Y. Zhu, Y. Chen, L. Fu, L. Liu, N. Yu, Y. Wu and T. Ree, In Pursuit of a Dendrite-Free Electrolyte/Electrode Interface on Lithium Metal Anodes: A Minireview, *Energy Fuels*, 2020, **34**, 10503–10512.
13 X. Xu, X. Yue, Y. Chen and Z. Liang, Li Plating Regulation on Fast-Charging Graphite Anodes by a Triglyme-$LiNO_3$ Synergistic Electrolyte Additive, *Angew. Chem., Int. Ed.*, 2023, **62**, e202306963.
14 M. Zhu, X. Zheng, L. Li, X. Zhu, Z. Huang, G. Wang, Y. Zhang, H. Liu, F. Yu, L. Wen, H. Liu, S. Dou and C. Wu, Towards stable sodium metal battery with high voltage output through dual electrolyte design, *Energy Storage Mater.*, 2022, **48**, 466–474.
15 Y. Zhao, L. V. Goncharova, Q. Zhang, P. Kaghazchi, Q. Sun, A. Lushington, B. Wang, R. Li and X. Su, Inorganic-Organic Coating *via* Molecular Layer Deposition Enables Long Life Sodium Metal Anode, *Nano Lett.*, 2017, **17**, 5653–5659.
16 L. Fan and X. Li, Recent advances in effective protection of sodium metal anode, *Nano Energy*, 2018, **53**, 630–642.

17 D. Wu, J. He, J. Liu, M. Wu, S. Qi, H. Wang, J. Huang, F. Li, D. Tang and J. Ma, Li_2CO_3/LiF-Rich Heterostructured Solid Electrolyte Interphase with Superior Lithiophilic and Li^+-Transferred Characteristics *via* Adjusting Electrolyte Additives, *Adv. Energy Mater.*, 2022, **12**, 2200337.

18 Q. Ni, Y. Xiong, Z. Sun, C. Sun, Y. Li, X. Yuan, H. Jin and Y. Zhao, Rechargeable Sodium Solid-State Battery Enabled by *In Situ* Formed Na-K Interphase, *Adv. Energy Mater.*, 2023, **13**, 2300271.

19 Y. Jin, Q. He, G. Liu, Z. Gu, M. Wu, T. Sun, Z. Zhang, L. Huang and X. Yao, Fluorinated $Li_{10}GeP_2S_{12}$ Enables Stable All-Solid-State Lithium Batteries, *Adv. Mater.*, 2023, **35**, 2211047.

20 Z. Tai, Y. Liu, Z. Yu, Z. Lu, O. Bondarchuk, Z. Peng and L. Liu, Non-collapsing 3D solid-electrolyte interphase for high-rate rechargeable sodium metal batteries, *Nano Energy*, 2022, **94**, 106947.

21 X. Liu, Q. Lu, A. Yang and Y. Qian, High ionic conductive protection layer on Zn metal anode for enhanced aqueous zinc-ion batteries, *Chin. Chem. Lett.*, 2023, **34**, 107703.

22 X. Zhang, F. Hao, Y. Cao, Y. Xie, S. Yuan, X. Dong and Y. Xi, Dendrite-Free and Long-Cycling Sodium Metal Batteries Enabled by Sodium-Ether Cointercalated Graphite Anode, *Adv. Funct. Mater.*, 2021, **31**, 2009778.

23 J. Yan, G. Zhi, D. Kong, H. Wang, T. Xu, J. Zang, W. Shen, J. Xu, Y. Shi, S. Dai, X. Li and Y. Wang, 3D printed rGO/CNT microlattice aerogel for a dendrite-free sodium metal anode, *J. Mater. Chem. A*, 2020, **8**, 19843–19854.

24 S. Chi, X. Qi, Y. Hu and L. Fan, 3D Flexible Carbon Felt Host for Highly Stable Sodium Metal Anodes, *Adv. Energy Mater.*, 2018, **8**, 1702764.

25 Z. Xu, Z. Guo, R. Madhu, F. Xie, R. Chen, J. Wang, M. Tebyetekerwa, Y. Hu and M. Titirici, Homogenous metallic deposition regulated by defect-rich skeletons for sodium metal batteries, *Energy Environ. Sci.*, 2021, **14**, 6381–6393.

26 L. Ding, X. Yue, X. Zhang and Z. Liang, A polyimine aerogel separator with electron cloud design to boost Li-ion transport for stable Li metal batteries, *Pnas*, 2023, **120**, e2314264120.

27 W. Bi, G. Gao, C. Li, G. Wu and G. Cao, Synthesis, properties, and applications of MXenes and their composites for electrical energy storage, *Prog. Mater. Sci.*, 2024, 142.

28 M. Wang, B. Qin, S. Wu, Y. Li, C. Liu, Y. Zhang, L. Zeng and H. Fan, Interface ion-exchange strategy of MXene@$FeIn_2S_4$ hetero-structure for super sodium ion half/full batteries, *J. Colloid Interface Sci.*, 2023, **650**, 1457–1465.

29 X. Hui, X. Ge, R. Zhao, Z. Li and L. Yin, Interface Chemistry on MXene-Based Materials for Enhanced Energy Storage and Conversion Performance, *Adv. Funct. Mater.*, 2020, **30**, 2005190.

30 C. Wei, Y. Tao, Y. An, Y. Tian, Y. Zhang, J. Feng and Y. Qian, Recent Advances of Emerging 2D MXene for Stable and Dendrite-Free Metal Anodes, *Adv. Funct. Mater.*, 2020, **30**, 2004613.

31 M. Greaves, S. Barg and M. A. Bissett, MXene-Based Anodes for Metal-Ion Batteries, Batteries Supercaps, *Batteries Supercaps*, 2020, **3**, 214–235.

32 J. Luo, X. Tao, J. Zhang, Y. Xia, H. Huang, L. Zhang, Y. Gan, C. Liang and W. Zhang, Sn^{4+} Ion Decorated Highly Conductive Ti_3C_2 MXene: Promising Lithium-Ion Anodes with Enhanced Volumetric Capacity and Cyclic Performance, *ACS Nano*, 2016, **10**, 2491–2499.

33 Q. Lu, C. Liu, Y. Zhao, W. Pan, K. Xie, P. Yue, G. Zhang, A. Omar, L. Liu, M. Yu and D. Mikhailova, Freestanding MXene-based macroforms for electrochemical energy storage applications, *SusMat*, 2023, **3**, 471–497.

34 J. Wang, Z. Zhang, X. Yan, S. Zhang, Z. Wu, Z. Zhuang and W. Han, Rational Design of Porous N-Ti_3C_2 MXene@CNT Microspheres for High Cycling Stability in Li-S Battery, *Nanomicro Lett.*, 2019, **12**, 4.

35 Y. Song, Z. Sun, Z. Fan, W. Cai, Y. Shao, G. Sheng, M. Wang, L. Song, Z. Liu, Q. Zhang and J. Sun, Rational design of porous nitrogen-doped Ti_3C_2 MXene as a multifunctional electrocatalyst for Li–S chemistry, *Nano Energy*, 2020, **70**, 104555.

36 Y. Wu, P. Nie, J. Wang, H. Dou and X. Zhang, Few-Layer MXenes Delaminated *via* High-Energy Mechanical Milling for Enhanced Sodium-Ion Batteries Performance, *ACS Appl. Mater. Interfaces*, 2017, **9**, 39610–39617.

37 J. Luo, C. Wang, H. Wang, X. Hu, E. Matios, X. Lu, W. Zhang, X. Tao and W. Li, Pillared MXene with Ultralarge Interlayer Spacing as a Stable Matrix for High Performance Sodium Metal Anodes, *Adv. Funct. Mater.*, 2019, **29**, 1805946.

38 J. Luo, X. Lu, E. Matios, C. Wang, H. Wang, Y. Zhang, X. Hu and W. Li, Tunable MXene-Derived 1D/2D Hybrid Nanoarchitectures as a Stable Matrix for Dendrite-Free and Ultrahigh Capacity Sodium Metal Anode, *Nano Lett.*, 2020, **20**, 7700–7708.

39 Y. Dong, Z. Wu, S. Zheng, X. Wang, J. Qin, S. Wang, X. Shi and X. Bao, Ti_3C_2 MXene-Derived Sodium/Potassium Titanate Nanoribbons for High-Performance Sodium/Potassium Ion Batteries with Enhanced Capacities, *ACS Nano*, 2017, **11**, 4792–4800.

40 M. Shekhirev, C. E. Shuck, A. Sarycheva and Y. Gogotsi, Characterization of MXenes at every step, from their precursors to single flakes and assembled films, *Prog. Mater. Sci.*, 2021, **120**, 100757.

41 X. He, S. Jin, L. Miao, Y. Cai, Y. Hou, H. Li, K. Zhang, Z. Yan and J. Chen, A 3D Hydroxylated MXene/Carbon Nanotubes Composite as a Scaffold for Dendrite-Free Sodium-Metal Electrodes, *Angew. Chem., Int. Ed.*, 2020, **59**, 16705–16711.

42 T. Ma, J. Cao, M. Jaroniec and S. Qiao, Interacting Carbon Nitride and Titanium Carbide Nanosheets for High-Performance Oxygen Evolution, *Angew. Chem., Int. Ed.*, 2016, **55**, 1138–1142.

43 J. Huang, R. Meng, L. Zu, Z. Wang, N. Feng, Z. Yang, Y. Yu and Ji. Yang, Sandwich-like $Na_{0.23}TiO_2$ nanobelt/Ti_3C_2 MXene composites from a scalable *in situ* transformation reaction for long-life high-rate lithium/sodium-ion batteries, *Nano Energy*, 2018, **46**, 20–28.

44 Y. Cao, Q. Deng, Z. Liu, D. Shen, T. Wang, Q. Huang, S. Du, N. Jiang, C. Lin and J. Yu, Enhanced thermal properties of poly(vinylidene fluoride) composites with ultrathin nanosheets of MXene, *RSC Adv.*, 2017, **7**, 20494–20501.

45 X. Zhang, R. Lv, A. Wang, W. Guo, X. Liu and J. Luo, MXene Aerogel Scaffolds for High-Rate Lithium Metal Anodes, *Angew. Chem., Int. Ed.*, 2018, **57**, 15028–15033.